Single-shot depth profiling by spatio-temporal encoding with a multimode fiber

SZU-YU LEE,[1,2,4] **PUI-CHUEN HUI,**[1,4] **BRETT BOUMA,**[1,2,3] **AND MARTIN VILLIGER**[1,5]

[1]*Harvard Medical School and Massachusetts General Hospital, Wellman Center for Photomedicine, Boston MA 02114, USA*
[2]*Harvard-MIT Health Sciences and Technology, Massachusetts Institute of Technology, Cambridge MA 02139, USA*
[3]*Institute for Medical Engineering and Science, Massachusetts Institute of Technology, Cambridge MA 02139, USA*
[4]*These authors contributed equally to this article*
[5]*mvilliger@mgh.harvard.edu*

Abstract: Computational imaging with random encoding patterns obtained by scattering of light in complex media has enabled simple imaging systems with compelling performance. Here, we extend this concept to axial reflectivity profiling using spatio-temporal coupling of broadband light in a multimode fiber (MMF) to generate the encoding functions. Interference of light transmitted through the MMF with a sample beam results in path-length-specific patterns that enable computational reconstruction of the axial sample reflectivity profile from a single camera snapshot. Leveraging the versatile nature of MMFs, we demonstrate depth profiling with bandwidth-limited axial resolution of 13.4 µm over a scalable sensing range reaching well beyond one centimeter.

1. Introduction

Integration of computational reconstruction into the process of image formation can offer increased measurement flexibility compared to conventional imaging systems whose performance generally depends on well-engineered optics [1,2]. Shifting accurate design requirements from the optical and mechanical domains to the entire imaging process including computational reconstruction may drastically mitigate physical measurement limitations and stimulate the advent of simpler or more efficient imaging systems [1,3]. Complex or disordered media that generate random patterns to serve as encoding functions for computational reconstruction have been shown to enable imaging with improved lateral resolution [4–6], extended field of view [4,7], increased depth of focus [8], of 3D objects [9,10], at multiple wavelengths [11], with higher frame-rate [12], or at X-ray wavelength [13], which otherwise cannot be achieved without substantially more sophisticated hardware. In a similar fashion, random temporal fluctuations have been exploited for temporal ghost imaging [14–17].

A convenient way to generate suitable random encoding functions in the spatial, temporal, spectral, and polarization domains is by repurposing multimode fiber (MMF) as a complex medium with ultra-small form factor [18,19]. When illuminated from one end, a random, albeit deterministic speckle pattern emerges at the other end. The number of modes within the MMF defines the number of independent patterns that are available and that, if known a priori, can serve as random encoding functions [19–24]. For instance, lateral spatial encoding with MMFs has enabled ultra-thin wide-field endoscopy [20,21,23]. Similarly, the MMF's spatio-spectral coupling has been employed for high resolution spectrometry with a broad sensing range [22,24], and recently also for temporal profiling [25]. Despite these advances, strategies for encoding the axial dimension are missing.

Here we demonstrate a new strategy for axial reflectivity profiling by computational coherence gating with micron-scale resolution and centimeter-long sensing depth. Using broadband light, the closely spaced yet distinct propagation constants of the MMF's various spatio-temporal modes yield a set of spatially distributed encoding functions that serve for depth referencing. Interference with a sample signal that is delayed by reflection at a specific sample depth only occurs for the path-length-matched encoding function, creating a distinct speckle pattern unique to this exact depth position. A general one-dimensional (1D) sample reflectivity profile produces the linear superposition of the associated speckle patterns. By calibrating the random encoding functions, the 1D sample depth profile can be computationally reconstructed from a single recording of the interference pattern without the need for any mechanical or optical scanning. This configuration can be considered as parallel ghost imaging in time, or spatially multiplexed low-coherence interferometry, and is a parallel and computational implementation of ghost optical coherence tomography [26]. We demonstrate proof-of-concept axial profiling with a sensing depth range scaling from several millimeters to well beyond one centimeter by varying the physical length of the MMF, relaxing the challenging hardware requirements of achieving similar performance with conventional spectrometer-based coherence gating.

2. Methods

As shown in Fig. 1, light from a short-temporal-coherence broadband source (65 nm full width at half maximum (FWHM)) centered at 1290 nm is split into a sample and a reference arm. In the sample arm, light is guided through single mode fiber (SMF) and a circulator to a sample, with an average power of 3.8 mW after collimation. The same fiber receives the backscattered light that is coupled back into the same single spatial mode. In the reference arm, light is guided through SMF and a circulator to reflect off a gold-coated mirror. The light coupled back into the same single spatial mode is then delivered to a segment of step-index MMF ($\emptyset = 105\,\mu m$, 0.22 NA, Thorlabs). Light emerging from the SMF in the sample arm and the MMF in the reference arm interferes in an off-axis configuration for holographic recording, where the reference light is offset by a chromatic phase tilt with respect to the sample light by means of a plane ruled reflective blazed grating (60 lines/mm, Richardson Gratings). Only the first diffracted order of the reference light is intercepted to interfere with the sample light. Each wavelength in the reference arm receives from the grating the same offset in transverse momentum, thereby resulting in a modulated interference pattern with a constant modulation frequency independent of wavelength. The modulated interference pattern is recorded with an InGaAs camera (OW1.7-VS-CL-LP-640, Raptor Photonics) with an integration time of 2 ms after passing through a linear polarizer. Digital processing of each captured frame isolates one of the two complex-valued interference terms directly in the in-plane momentum domain within a circular aperture of radius k_r and offset from the zero frequency by k_0. Whereas k_r is imposed by the numerical aperture (NA) of the MMF, k_0 comes from the grating-induced phase tilt. The single detected polarization state corresponds to ~790 theoretically available modes in the MMF. In our experiments, MMF segments of 206 cm, 54 cm, or 54 + 152 cm in length have been used in the reference arm.

Due to the short-temporal-coherence source, the sample light from depth z only interferes with the guided modes in the reference arm that have matching path length $2z$. The interference patterns, v_s, can be modeled as

$$v_s(k_x, k_y) = \iint A(k)dkdz \cdot \sum_n \varphi_n(k_x, k_y, k)e^{i\beta_n(k)L} \cdot f(z) \cdot e^{-2ikz}, \tag{1}$$

which describes the interaction between the reflectivity profile $f(z)$ and the guided modes φ_n as a function of coordinates in the in-plane momentum domain, k_x, k_y and wavenumber k with corresponding propagation constants β_n traveling along a MMF with physical length L. $A(k)$ is the source power spectrum. The model ignores modal cross-talk along the fiber. In
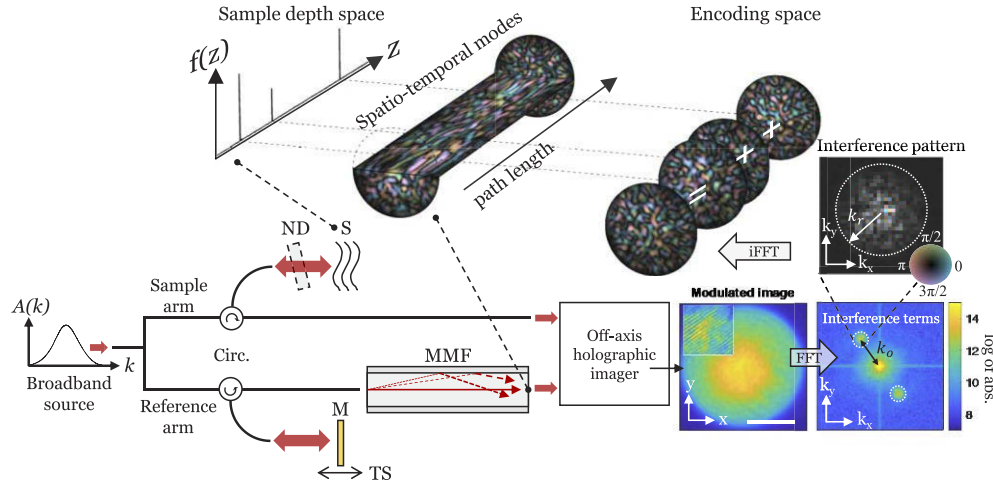
Fig. 1. Schematic view of the axial profiling system with MMF-generated random encoding functions. Circ.: Circulator. M: Mirror. TS: Translational stage. ND: Neutral density filter (only present in MMF calibration and characterization phases). S: Sample. All light coupled from fiber to free space is collimated. The off-axis holographic imager comprises image relay optics, a reflective grating, and a camera. The MMF facet is relayed onto the reflective grating for chromatic phase offsetting, and the first-order diffracted light is relayed onto the camera. In the other interferometer arm, the sample light is expanded before combination with the reference light to match the image of the MMF facet for holographic recording. The inset panels show a modulated interference pattern in pixels in the camera coordinates and in the in-plane momentum domain, respectively. The scale bar in the inset is 50 μm. The off-axis configuration allows isolating one of the two interference terms directly in the momentum domain to define a random encoding function during the REM calibration phase (sample is a mirror) or to encode the sample depth profile during imaging. The color map encodes complex values.

this study, we measured the interference pattern directly in the in-plane momentum domain and converted it into a column vector for image reconstruction. During an initial calibration procedure, interference patterns are recorded for varying path length offsets between a gold-coated mirror in the sample arm and the reference arm mirror, which is translated with a stepping stage (SGSP20-20, Sigma-Koki) at a sampling step size dz. A neutral density filter, measured to provide 32.7 dB double-pass attenuation, was inserted in the sample arm to avoid camera saturation. Each interference pattern corresponds to an independent realization of a random speckle pattern if its path length differs by more than the source coherence length from other path lengths. To guarantee a continuous sensing range, dz was set below the coherence length. Rearranging column by column the ensemble of vectorized random encoding functions recorded over the translation range of the stepping stage provides a random encoding matrix (REM) that represents the linear transformation from the sample depth space to the encoding space. An example of a calibrated REM obtained with a 54 cm long MMF in the reference arm and $dz = 10$ μm as well as a few constituent random encoding functions are shown in Figs. 2(a) and 2(b).

Mathematically, the 1D reflectivity depth profile of the sample v_d is transformed by the random encoding functions that constitute the REM into a column vector v_s:

$$v_s = M_{REM} \times v_d, \qquad (2)$$

where v_s is obtained by vectorizing the measured sample interference pattern in the momentum domain acquired from a single camera snapshot. To analytically reconstruct an estimate of the

underlying sample reflectivity profile, ideally, we would need the inverse of the REM. However, the true inverse of a matrix only exists when the matrix is non-singular. Our measured REM, in general, is non-square and is further corrupted by noise. As a result, we resorted to signal reconstruction by using approximated matrix inversion such as Hermitian transpose or Tikhonov regularization. The Tikhonov regularization parameter was chosen as 7% of the greatest singular value based on Picard plot, L-curve, and generalized cross-validation methods [27].
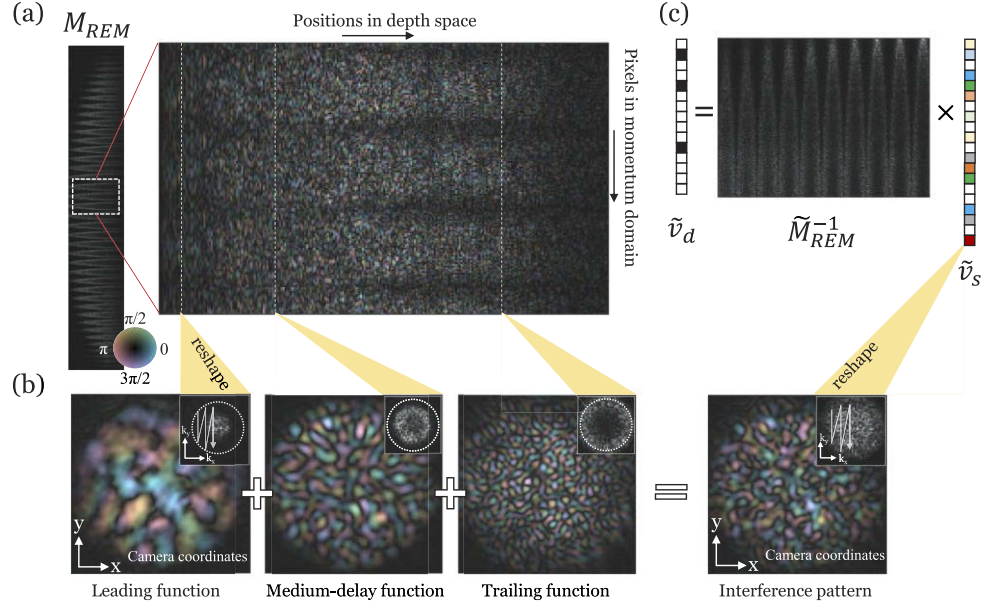

Fig. 2. (a) An experimental random encoding matrix (REM) with rows indexed in the vectorized momentum domain and columns indexed in the axial sample positions ($dz = 10$ μm). The color map encodes complex values. (b) Three examples of random encoding functions. By transforming the interference term from the momentum domain back to camera coordinates, we can visualize the spatial profile of the corresponding random encoding function. The inset of each function shows the interference term in the momentum domain, which is vectorized to form a column of the calibrated REM. The leading function comprises low-order guided modes that experience the shortest path length and encode shallow sample depth. In contrast, the trailing function comprises high-order guided modes, which experience a longer path length and encode deeper sample information. (c) Obtained by a single snapshot, an REM-encoded reflectivity profile is represented by a column vector $\tilde{v}_s$, which is a vectorized interference pattern in the momentum domain that equals the superposition of random encoding functions weighted by the reflectivity profile, and tilde indicates the measured quantities. The corresponding complex field in camera coordinates is also shown. Applying the approximated inversion of the calibrated REM, $\tilde{M}_{REM}$, to the column vector $\tilde{v}_s$ reconstructs the 1D reflectivity profile $\tilde{v}_d$.

To see how the light coupled into the MMF in the reference arm populates different guided modes, we computed the energy of individual random encoding functions, which corresponds to the square of the Euclidean norm of the column vectors in the calibrated REM. The energy trace visualizes the energy distribution among the random encoding functions. We interpreted the axial range within 1% to 99% of the total axially integrated energy as the axial sensing depth range. Moreover, SVD analysis of the calibrated REM enables inspection of the available degrees of freedom. The 7% cutoff from the Tikhonov regularization determines the number of meaningful singular values, which is related to the number of populated guided modes. We further defined as

a sensitivity matrix (S Matrix) the product of the approximated inverse of the REM with a second identically but independently calibrated REM. The columns of the sensitivity matrix reveal the axial position of the calibration mirror for each recorded position, subject to both calibration and measurement noise. Hence, the sensitivity matrix should be close to the identity matrix such that the reconstructed sample depth profile corresponds to the ground truth. The properties of the sensitivity matrix entirely define the performance of the depth profiling system. The on-diagonal energy of the sensitivity matrix reveals the system's signal roll-off, specifying how fast the signal level drops with increasing depth owing to the larger propagation loss of higher-order modes. On the other hand, the off-diagonal elements of the sensitivity matrix define the background signal, composed of residual correlations and noise. For quantitative evaluation, we averaged the energy of the matrix elements in the off-diagonal bands separated 2 to 8 coherence lengths from the matrix diagonal in row-wise direction. The ratio between the on-diagonal and the off-diagonal energy of the sensitivity matrix at an axial position expresses the signal-to-noise ratio (SNR) of the attenuated mirror reflection at that depth. Considering the double-pass attenuation of the neutral density filter, 32.7 dB, offers a measure of system sensitivity by comparing the noise level to the hypothetical signal of a perfect reflector.

3. Results

To leverage the random encoding functions generated by a MMF for imaging axial reflectivity profiles, it is crucial to understand how the spatio-temporal coupling and modal delay in the fiber structure the REM. To investigate these characteristics, with the neutral density filter and the gold-coated mirror placed in the sample arm, we examined the energy distribution, the sensitivity matrix, and residual correlation among the encoding functions while varying physical parameters such as coupling regime, mode mixing, and MMF length, before performing proof-of-principle sample imaging of custom-made phantoms.

3.1. Coupling regimes and matrix inversion

First, we employed a 206 cm long MMF in the reference arm with light coupled concentrically, which we refer to as central coupling regime. In the energy trace in Fig. 3(a), the leading random encoding function from the fastest MMF-guided mode appears as a dominant signal peak at the beginning of the energy trace. The energy trace decays sharply afterwards, indicating that the fastest lower-order guided modes carry most of the coupled optical energy. The sensing depth range was calculated as 6.4 mm. The SVD analysis of the calibrated REM, which visualizes the amplitude of the singular values, found only 297 populated modes, many fewer than the ~790 available modes. This may be due to the fact that most light is coupled into lower-order modes in the launch condition. We then compared the sensitivity matrices obtained with the Hermitian transpose and Tikhonov-regularized reconstruction, respectively, and averaged the SNR within the first 6 mm of the available depth range. While the Hermitian transpose led to a rapid signal roll-off of −4.5 dB/mm and a low averaged SNR of 18.9 dB, Tikhonov-inversion offered a milder signal roll-off, −1.9 dB/mm, and a better averaged SNR of 26.0 dB. This suggests that the calibrated REMs are not even approximately unitary and numerically compensating for part of the experienced loss improves the reconstruction. We only used Tikhonov inversion for reconstruction of depth profiles and computation of the sensitivity matrix hereafter.

In the central coupling regime, the sensing depth range was confined due to the limited number of populated modes. To promote the population of higher-order modes, we coupled light into the MMF through two layers of Scotch tape, added into the fiber connector, to weakly scatter the transmitted light and excite higher-order modes. We termed this launch condition speckle coupling regime. Although this, indeed, resulted in increased coupling to higher-order modes, the resulting energy trace was very uneven. To homogenize the energy distribution between the guided modes, we further induced mode mixing along the MMF with a fiber mode scrambler
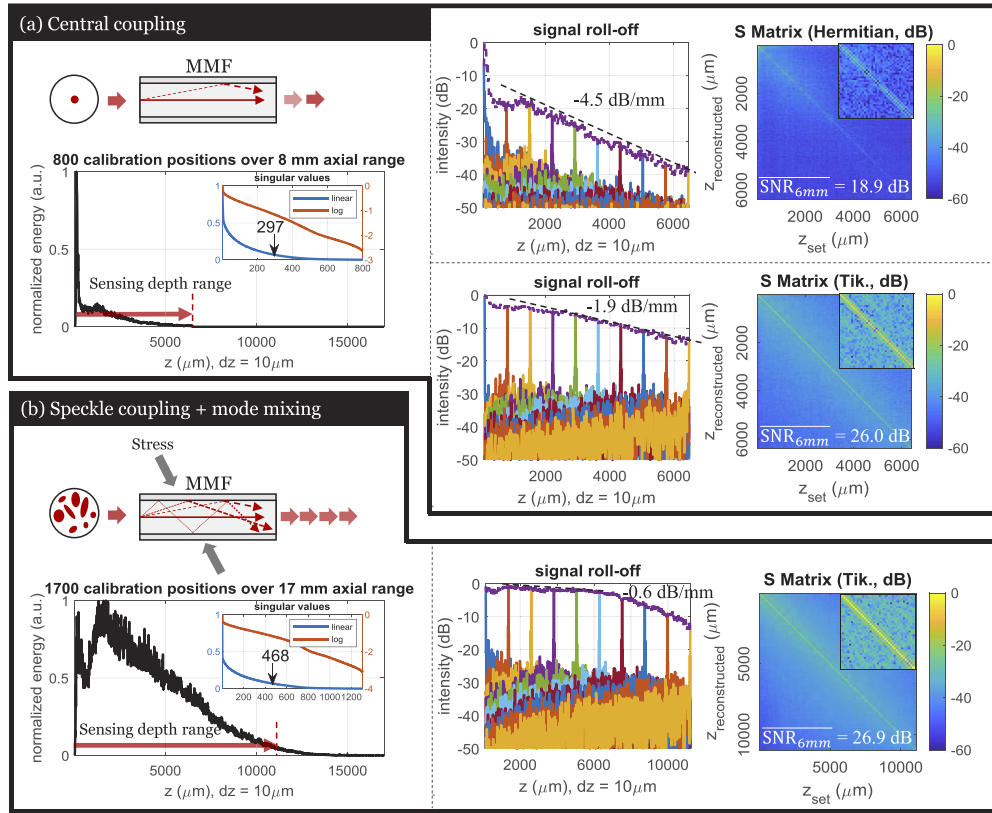
Fig. 3. Analysis of system performance under different operating regimes. (a) Under the central coupling regime, a limited number of guided modes is populated, as also revealed by the singular values of the measured REM (inset). If we use 7% as a cutoff value in the SVD, there are 297 guided modes populated. The sensing depth range is 6.4 mm. The Tikhonov inversion outperforms the Hermitian inversion by improving the averaged SNR over the first 6 mm from 18.9 dB to 26.0 dB. (b) Under the speckle coupling regime and mode mixing, 468 modes are populated according to the SVD analysis. Also, the energy distribution among the random encoding functions is more uniform compared to that in the central coupling regime, leading to a sensing depth range of 11.1 mm . The signal level decays at a much slower rate. Finally, the averaged SNR over the first 6 mm is 26.9 dB. The inset of sensitivity matrix (S Matrix) shows a magnified central section. The sampling step size in both cases was 10 μm.

(FM-1, Newport). While mode scrambling with the central coupling regime offered better energy distribution than without scrambling, we found the combination of both speckle coupling regime and scrambling to be the most efficient for obtaining a smooth energy distribution. As shown in Fig. 3(b), with the speckle coupling regime and mode mixing, the energy was more uniformly distributed among the available random encoding functions, thereby extending the sensing depth range to 11.1 mm. SVD analysis revealed 468 populated modes. Furthermore, we found a signal roll-off of only −0.6 dB/mm within the first 6 mm depth range, much smaller than that in the central coupling regime. Inspecting the sensitivity matrix, the averaged SNR was slightly improved to 26.9 dB. In the following experiments, we used the speckle coupling regime and applied mode scrambling to optimize the sensing depth range and SNR.

3.2.   Bandwidth-limited axial resolution

The resolving power to differentiate axially offset reflections depends on how fast the encoding functions decorrelate as a function of depth. We computed the function correlation matrix (FCM) as the normalized correlation between the encoding functions, E, at individual axial positions z_1 and z_2 as

$$C(z_1, z_2) \equiv \frac{\int E(k_{x,y}, z_1) \cdot E^*(k_{x,y}, z_2) dk_{x,y}}{\sqrt{\int |E(k_{x,y}, z_1)|^2 dk_{x,y}} \cdot \sqrt{\int |E(k_{x,y}, z_2)|^2 dk_{x,y}}}, \tag{3}$$

where the superscript * indicates complex conjugation. We measured random encoding functions at a sampling step size of 1 µm over a 200 µm axial range both for a 206 cm and 54 cm long MMF in the reference arm and calculated the resulting correlations. Because of phase drift in the interferometer, there exist random phase offsets between the various measured encoding functions. However, owing to the close correlation in these densely sampled encoding functions, it is straightforward to estimate and correct for the phase offsets.

By analyzing correlation traces $C(z_1, \Delta z)$ of the FCM in terms of the axial offset $\Delta z = z_1 - z_2$ we can assess the system resolving power. Figure 4 shows the average real part of correlation traces across the evaluated axial range, exhibiting FWHMs of 19 µm and 16 µm, respectively, for (a) 206 cm and (b) 54 cm long MMF. The obtained correlation traces exhibit a slight variation as a function of depth z_1, more so for the longer MMF. Nevertheless, they remain remarkably constant and can be approximated as the autocorrelation of the axial point spread function (PSF) of the profiling system, given by the Fourier transformation of the source spectrum, i.e. its axial coherence function. The autocorrelation of the coherence function indeed closely matches the central peak of the experimental FCM, suggesting that the axial resolution is bandwidth-limited. Considering the close-to-Gaussian shape of the employed spectrum, the FWHM of the correlation peak is $\sqrt{2}$ times the width of the underlying PSF and we estimated the axial resolution to be 13.4 µm and 11.3 µm for the 206 cm and 54 cm long MMF, respectively. In contrast to the coherence function, the real part of the experimental correlation traces feature quite prominent sidelobes, which are of negative sign, as disclosed in the phase maps shown in Fig. 4. This may be attributed to spectral distortion in either arm of the interferometer that impacts the originally close to ideal shape of the spectrum.

3.3.   Scalable sensing depth range and residual function correlation

The available degrees of freedom are determined by the number of populated modes, which can be controlled by tailoring the input coupling regime and mode-mixing process. Meanwhile, the axial resolution is determined by the decorrelation distance between random encoding functions, which corresponds to the temporal coherence length of the source. Dividing the sensing depth range by the decorrelation distance provides the number of resolvable depth positions. To investigate the relation between the number of degrees of freedom and resolvable depth positions in more detail, we conducted experiments with a 54 cm MMF and a 152 cm MMF, concatenated to the 54 cm fiber. In the first experiment, the 54 cm MMF was used alone, while in the second experiment, the 54 cm MMF was concatenated with the 152 cm MMF through a conventional FC/PC fiber connector (ADAFCB1, Thorlabs), resulting in a total MMF length of 206 cm. To populate a multitude of guided modes and homogenize the energy distribution among random encoding functions, we employed the speckle coupling regime and induced mode mixing with the fiber mode scrambler in the common 54 cm MMF in both experiments. The additional 152 cm MMF in the second experiment was loosely looped and placed on the optical table to avoid additional strong modal interactions and energy exchange during light propagation.

As shown in Fig. 5, the 54 cm and 206 cm MMF offered 3.25 mm and 13.4 mm sensing depth range, respectively, corresponding to 288 and 1000 resolvable depth positions. In contrast, SVD analysis of the calibrated REMs indicated 346 and 660 degrees of freedom, respectively. The
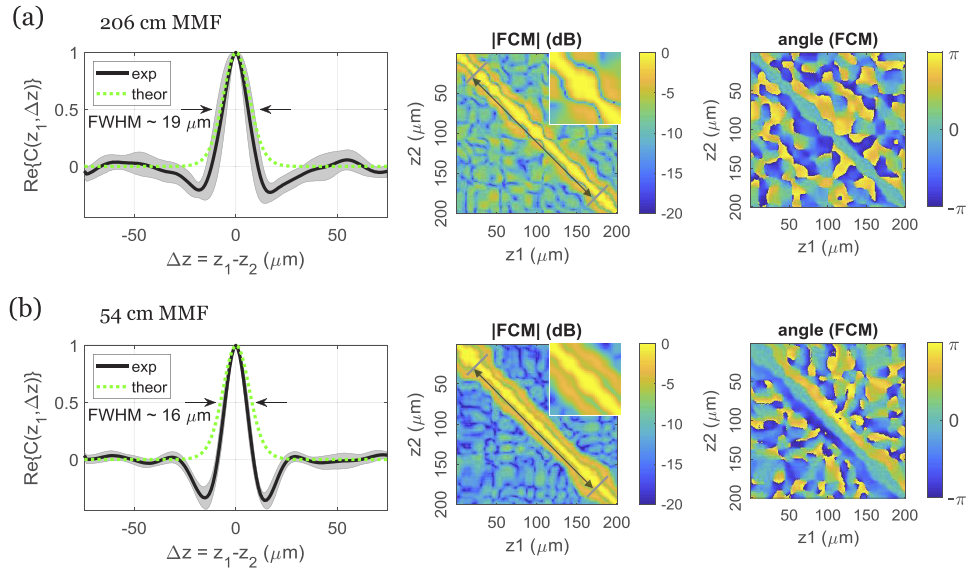
(a)

(b)

Fig. 4. Experimental demonstration of bandwidth-limited axial resolution. Correlations between the random encoding functions obtained with a (a) 206 cm and (b) 54 cm long MMF. Each column of the FCM corresponds to a correlation trace at depth z_1 and, hence, the auto-correlation of the axial PSF. The Re{·} means the average real part of arguments, and the black curves are the aligned correlation traces averaged over the evaluated axial range indicated by the black double-sided arrows, and the shaded area indicates the standard deviation. The green curves are the theoretical correlation traces generated by Fourier transforming the elemental-wise square of the source spectrum. The inset shows the magnified central area of the FCM. The sampling step size in both cases was 1 μm.

average SNR over the first 3 mm in the sensitivity matrix is 45.6 dB for the 54 cm MMF, much higher than the 27.1 dB for the 206 cm MMF. This suggests a trade-off between sensing depth range and average SNR. Furthermore, inspecting the constructed FCMs, we find that the 206 cm MMF resulted in a higher residual correlation, 0.0792, defined as the averaged correlation of off-diagonal elements within 2 to 30 coherence lengths away from the diagonal of the FCM. A higher residual correlation indicates more off-target signals that contribute to the background signal, which compromises the SNR. Consequently, increasing the number of resolvable depth positions beyond the number of available degrees of freedom comes at the expense of reducing system sensitivity. The experimental results are summarized in Table 1.

Table 1. Trade-off between sensing depth range and SNR

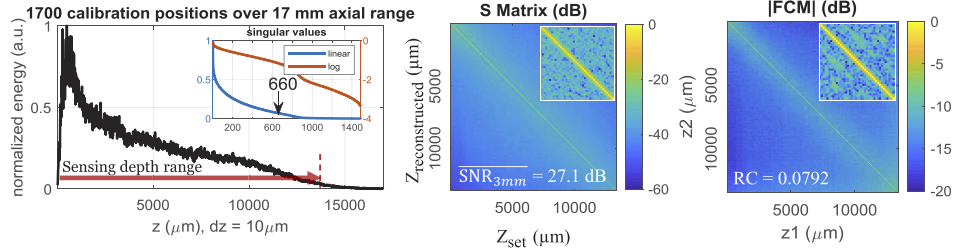|	$L = 54$ cm	$L = 206$ (=54 + 152) cm
Sensing depth range	3.25 mm	13.4 mm
Number of resolvable depth positions	288	1000
Degrees of freedom	346	660
Signal-to-noise ratio (SNR)[a]	45.6 dB	27.1 dB
Residual correlation	0.0561	0.0792

[a]SNR of a mirror, attenuated by 32.7 dB.
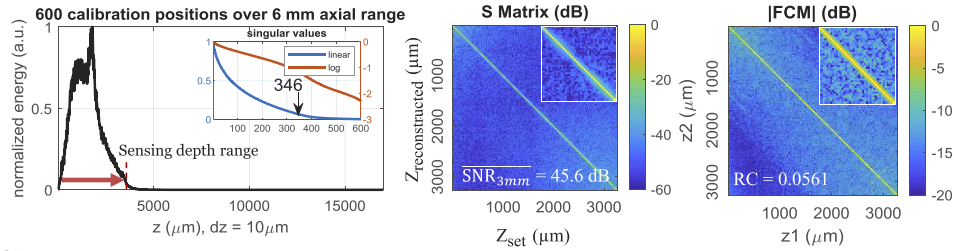
Fig. 5. Comparison of the sensing depth range, system SNR, and residual correlation between a (a) 54 cm and (b) 206 cm long MMF. (a) The 54 cm MMF had a limited sensing depth range of 3.25 mm. In the constructed sensitivity matrix, an increased noise floor in axial locations with low energy coupling is noticeable. (b) 206 cm MMF length leads to an extended sensing depth range of 13.4 mm yet a lower averaged SNR. Comparing the FCMs of the 206 cm MMF to that of the 54 cm MMF, besides a higher residual correlation, correlation at large axial offsets is also stronger. The sampling step size in both cases was 10 μm.

3.4. Depth profiling by a random encoding matrix

Finally, we demonstrate 1D depth profiling and two-dimensional (2D) cross-sectional imaging of custom-made phantoms placed in the sample arm. The samples consisted of stacks of glass slides, spaced by air gaps of different thickness. To optimize the efficiency of sample light collection, the specular reflections from sample interfaces were aligned with the illumination. We chose to fabricate these samples for profiling tests because the true physical locations of air-glass reflective interfaces were readily measurable as the ground truth for performance verification. Also, the air-glass interfaces acted as perfect Dirac delta functions for testing the system axial resolution.

For 1D depth profiling, the 206 cm MMF was used. The testing sample was a stack of two glass slides separated by a coverslip-thick air gap and with an overall physical thickness of about 2.3 mm, as shown in Fig. 6(a). Each single camera snapshot can be reconstructed into an entire depth profile, where the signal intensity indicates the sample reflectivity. As shown in Fig. 6(b), four clear signal peaks precisely mark the air-glass interface locations, as could be validated from the sample design. Furthermore, the FWHM of the signal peaks just slightly exceeds the sampling step size, 12 μm, consistent with the bandwidth-limited axial resolution.

To visually compare the imaging performance between use of short and long MMFs with their corresponding sensing depth ranges, we conducted cross-sectional 2D imaging of a 1D-structured sample with either the 54 cm or 206 cm MMF. In the experiment, an objective lens (LSM02, Thorlabs) for light focusing was inserted into the sample arm and in front of the sample, which comprised four glass slides separated by air gaps of different thickness and had an overall physical thickness of about 11 mm. A dispersion compensator (LSM02DC, Thorlabs) was inserted into the reference arm before the gold-coated mirror to compensate the chromatic dispersion
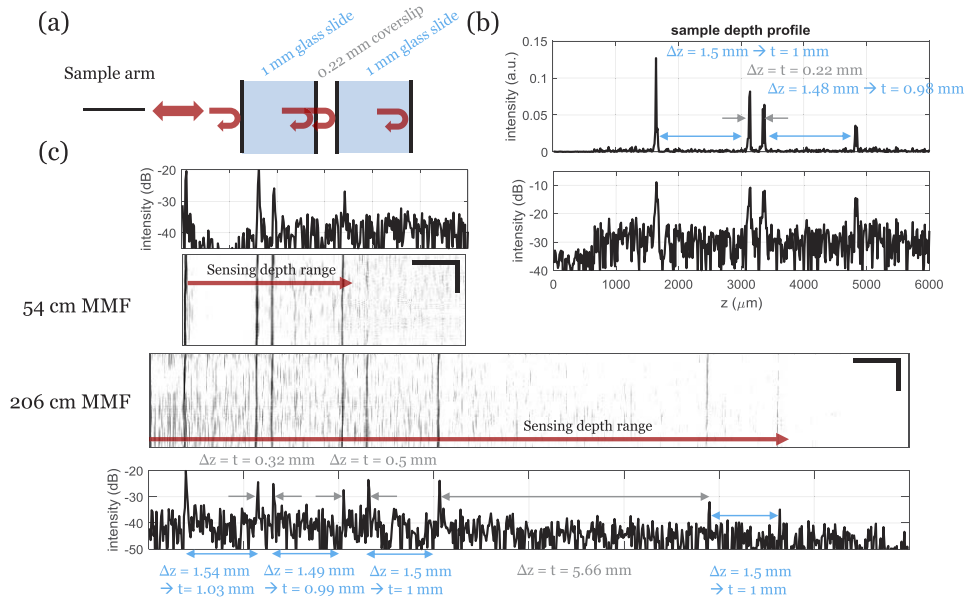
Fig. 6. Examples of sample depth profiling. (a) Schematic of the multi-layer sample. (b) The reconstructed depth profile shows four reflectivity peaks corresponding to the air-glass interfaces. The spacings between the peaks are consistent with the physical thickness of the glass slides and the coverslip when assuming a refractive index of glass of 1.5. The sampling step size was 12 μm. (c) Cross-sectional image of another sample acquired with either the 54 cm or the 206 cm MMF. For each case, a selected depth profile is plotted in log scale to show the relative intensity of sample reflectivity. Reflectivity peaks are consistent with physical locations of air-glass interfaces of the sample. Using the 206 cm MMF allows full-depth imaging of the sample yet suffers from inferior SNR compared to using the 54 cm MMF. The sampling step size in lateral and axial directions was 10 and 20 μm, respectively, and the scale bars are 1 mm.

introduced by the objective lens. The sample was translated in the lateral direction by a stepping stage (SGSP20-20, Sigma-Koki), and a camera snapshot to construct the corresponding depth profile was acquired at each lateral location. The sample and the scan range remained identical when switching between the two MMF lengths. As shown in Fig. 6(c), although the 54 cm MMF offered a limited depth range unable to cover the entire sample thickness, it provides superior SNR in the first 3 mm compared to the 206 cm MMF. On the other hand, despite the inferior SNR, the 206 cm MMF provided almost three-fold additional sensing depth range, enabling full-depth profiling of the sample.

4. Discussion

We presented a depth profiling system with micron-resolution and centimeter-long depth sensing range by performing computational coherence gating with random encoding functions generated from modal interference in a MMF. The ability to easily control the spatio-temporal coupling within the MMF affords a remarkable flexibility in adjusting the axial sensing range.

In theory, the physically available sensing depth range depends on the difference in the group delay between the fastest and the slowest guided mode. Based on geometric optics, with the fastest guided mode propagating parallel to the cylindrical axis and the slowest one zigzagging down the length of MMF at the critical angle $\theta_c = \sin^{-1}(n_2/n_1)$, where n_1 and $n_2 = n_1 - \Delta n$ are the refractive indices of the fiber core and the cladding, we can estimate the maximal sensing

depth range available with a given length of MMF L by their relative delay:

$$\Delta z_{max} \approx (^{n_1}/_{n_2}) \times \Delta n \times L. \tag{4}$$

With 206 cm or 54 cm long step-index MMFs, the maximal sensing depth ranges are 35 mm and 9.2 mm, respectively.

In our experiments, we first demonstrated that the sensing depth range and averaged SNR improve with the number of populated modes. While the speckle coupling regime and mode mixing help to populate higher-order modes, Tikhonov-inversion numerically corrects for unequal energy distribution among the random encoding functions. The Hermitian transpose is not an ideal reconstruction technique since the system is lossy and not unitary. Even with Tikhonov inversion, the achieved sensing depth range, 11.1 mm, is well below the theoretical lossless approximation of 35 mm for the 206 cm MMF. Several reasons can explain the restricted sensing depth range: The speckle input in the speckle coupling regime was not optimized to populate all guided modes (468 experimentally populated modes vs. 790 theoretically available modes). Mode mixing in the strong mode coupling regime, where light is coupled between guided modes of very different propagation constants, causes large path lengths to be averaged with shorter ones, thereby leading to a reduced sensing depth range [28]. Also, higher-order guided modes are more likely to experience propagation loss upon fiber deformation and scrambling, and coupling energy to random encoding functions at large pathlength offsets is challenging. Finally, the detection of a single polarization state likely leads to additional loss. Engineering the input wave front coupling into the MMF and employing full polarization detection may offer more uniform energy distribution.

The number of resolvable depth positions can be calculated as the sensing depth range divided by the decorrelation distance. Based on Eq. (4) and the source coherence length, the number of the maximal resolvable depth positions with 206 cm MMF is 3097, which is significantly larger than the total number of available guided modes, ~790 in a single polarization state. Since the delay of the random encoding functions is not continuous due to the discrete distribution of the propagation constants of the MMF's guided modes, it is conceivable that this would fragment the sensing range. However, we did not observe any discontinuity within the experimental energy trace or sensitivity matrix. This may suggest that sufficient mode mixing is taking place to maintain a continuous sensing range. Notwithstanding, our experiments revealed a trade-off between sensing depth range and sensitivity. When the number of resolvable depth positions exceeds the number of the REM's singular values with appreciable amplitude, the signal reconstruction becomes ill-conditioned and more sensitive to noise, as shown in Table 1. To operate the system in a well-conditioned regime, where its REM is highly invertible and the sensing depth range is maximized to use all degrees of freedom, the number of resolvable depth positions should match the degrees of freedom. Therefore, considering a MMF with all available modes equally populated, the optimal sensing depth range, Δz_{opt}, can be determined by the number of total available guided modes of a MMF, N_{mode}, and the source coherence length, l_{coh},

$$\Delta z_{opt} = N_{mode} \times l_{coh}. \tag{5}$$

Specifically, for the depth profiling system operating with the $\varnothing = 105$ μm, 0.22 NA MMF, the number of total available modes in a single polarization state is 790, and the optimal sensing depth range is 10.3 mm, which corresponds to 61 cm MMF according to Eq. (5), assuming all available modes are equally populated.

Our imaging strategy using random encoding functions generated by a MMF does not rely on sample sparsity. Although the properties of the generated encoding functions would likely be suitable for subsampling of sparse signals, the set of encoding functions spans the entire depth range, allowing direct inversion and, hence, reconstruction of the full depth information. However, digital post-processing for distortion compensation, aberration cancellation, or noise

suppression to improve measurement performance would be possible through refined inversion strategies and inclusion of regularization in the image reconstruction.

Using the random encoding functions obtained from complex media for computational imaging can circumvent physical constraints encountered by conventional imaging systems and facilitate the development of novel measurement architectures leading to smaller, faster, or cheaper devices. For instance, in a grating-based spectrometer for spectral-domain optical coherence tomography (SD-OCT), a large sensing range demands a diffraction grating with high spectral resolution, and the number of resolvable positions is linearly proportional to the dimension of the utilized line scan camera. A typical SD-OCT with millimeter sensing range and micron-scale axial resolution already employs line scan cameras with thousands of pixels. The specifications to enable centimeter imaging range with SD-OCT comparable to our depth-profiling system would be difficult to meet with commercially available line scan cameras. Previously, linear OCT has been proposed as a path to cheaper and simplified coherence gating by using spatial multiplexing. However, to achieve centimeter-long imaging range, it would still require a similar unpractically long linear image sensor or a sophisticated free-space interferometer [29,30]. While the initial implementation of our system used carefully designed achromatic off-axis holography, we verified experimentally that similar results can be obtained by simply tilting the MMF reference fiber, equivalent to replacing the reflective grating with an angled mirror (see Fig. 7). This suggests that even lens-less off-axis interference between the light from the single mode fiber and the MMF should result in comparable random encoding functions, offering a striking simplification of the system design. Indeed, the achromatic interference pattern is only needed when attempting to demodulate the broadband interference term into spatial camera coordinates. This is unnecessary for our sensing matrix which is constructed in the in-plane momentum domain, although extended bandwidth will radially blur the interference term and increase the number of elements in each column of the REM, eventually affecting the reconstruction stability.

5. Conclusions

In this paper, we introduced a depth profiling system that performs computational coherence gating by employing a set of random encoding functions generated from a MMF. The reflectivity at each axial position within a sample is encoded by interference with the corresponding random encoding function. With a calibrated REM, 1D reflectivity depth profiles of a sample can be non-adaptively reconstructed from a single camera snapshot without mechanical or optical scanning. Tailoring the physical length and coupling regime of the MMF, we demonstrated a scalable sensing depth range from 3.25 to 13.4 mm, while achieving high axial resolution of 13.4 μm. A sensing range exceeding the limit imposed by the available degrees of freedom in the MMF and the source coherence length comes at the expense of SNR in the reconstructed image. Our new approach to axial sample profiling may be useful in areas where a flexible trade-off between performance and system simplicity is beneficial, such as in industrial inspection, remote sensing, or medical imaging, and may inspire extension to two and three-dimensional imaging.
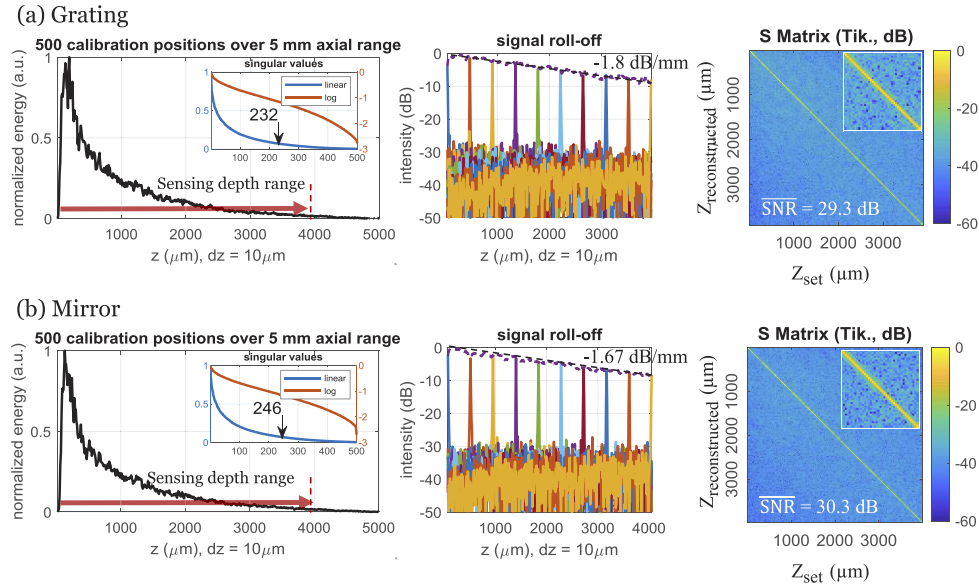
Fig. 7. Quantified system performance with (a) a reflective blazed grating or (b) a gold-coated mirror in the reference arm. In (a), the number of populated modes, sensing depth range, signal roll-off, and SNR is 232, 3.89 mm, −1.8 dB/mm, and 29.3 dB, respectively, whereas in (b), the values are 246, 3.98 mm, −1.67 dB/mm, and 30.3 dB. The slightly better system performance when using the gold-coated mirror in the reference arm may be due to its higher reflectivity compared to that of the grating.

Appendix

In the off-axis holographic imager of the experimental setup as shown in Fig. 1, a reflective blazed grating was employed to ensure a constant spatial modulation frequency for the recorded broadband interference pattern. This helps to generate fine interference fringes of high contrast across the entire recorded image when employing a short-temporal-coherence broadband source [31]. Nevertheless, the reflective grating and image relay optics increase the system complexity.

Here, we show that substituting the reflective blazed grating in the off-axis holographic imager with a tilted gold-coated mirror does not affect the system sensing range and sensitivity. In the reference arm, the 206 cm MMF with speckle coupling and mode mixing scrambler was used, and a flipping mirror was installed in front of the reflective blazed grating to allow switching between the grating and the gold-coated mirror. The angle of the gold-coated mirror was adjusted to reflect the reference light at the same angle as the first diffracted order of the grating, causing the same off-axis holography configuration for the central wavenumber. With the MMF coupling and shape unchanged, REMs for both conditions were measured individually by recording interference patterns for varying path length offsets between a gold-coated mirror in the sample arm and the reference arm mirror. By analyzing the REMs, as shown in Fig. 7, we find that the system performance is similar between the grating and the mirror. This suggests that encoding the sample depth profile directly in the in-plane momentum domain remains possible even when the interference patterns are chromatic. Therefore, the reflective blazed grating may not be necessary.

To streamline the depth profiling system, it may be possible to place the output ports of the reference MMF and the sample arm SMF in close proximity and directly in front of the camera without additional optical components. Thus, the reflective grating and image relay optics in the original system could be omitted, which may lead to a portable high-resolution and long-range

depth sensing device comprising only a broadband light source, SMFs, a pre-calibrated MMF, and a camera.

Disclosures

The authors declare no conflicts of interest.

References

1. J. N. Mait, G. W. Euliss, and R. A. Athale, "Computational imaging," Adv. Opt. Photonics **10**(2), 409 (2018).
2. M. P. Edgar, G. M. Gibson, and M. J. Padgett, "Principles and prospects for single-pixel imaging," Nat. Photonics **13**(1), 13–20 (2019).
3. M. F. Duarte, M. A. Davenport, D. Takhar, J. N. Laska, T. Sun, K. F. Kelly, and R. G. Baraniuk, "Single-pixel imaging via compressive sampling," IEEE Signal Process. Mag. **25**(2), 83–91 (2008).
4. Y. Choi, T. D. Yang, C. Fang-Yen, P. Kang, K. J. Lee, R. R. Dasari, M. S. Feld, and W. Choi, "Overcoming the diffraction limit using multiple light scattering in a highly disordered medium," Phys. Rev. Lett. **107**(2), 023902 (2011).
5. E. Mudry, K. Belkebir, J. Girard, J. Savatier, E. Le Moal, C. Nicoletti, M. Allain, and A. Sentenac, "Structured illumination microscopy using unknown speckle patterns," Nat. Photonics **6**(5), 312–315 (2012).
6. H. Yilmaz, E. G. van Putten, J. Bertolotti, A. Lagendijk, W. L. Vos, and A. P. Mosk, "Speckle correlation resolution enhancement of wide-field fluorescence imaging," Optica **2**(5), 424–429 (2015).
7. M. R. Rai, A. Vijayakumar, and J. Rosen, "Extending the field of view by a scattering window in an I-COACH system," Opt. Lett. **43**(5), 1043 (2018).
8. M. Liao, D. Lu, G. Pedrini, W. Osten, G. Situ, W. He, and X. Peng, "Extending the depth-of-field of imaging systems with a scattering diffuser," Sci. Rep. **9**(1), 7165 (2019).
9. A. K. Singh, D. N. Naik, G. Pedrini, M. Takeda, and W. Osten, "Exploiting scattering media for exploring 3D objects," Light: Sci. Appl. **6**(2), e16219 (2017).
10. N. Antipa, G. Kuo, R. Heckel, B. Mildenhall, E. Bostan, R. Ng, and L. Waller, "DiffuserCam: lensless single-exposure 3D imaging," Optica **5**(1), 1–9 (2018).
11. S. K. Sahoo, D. Tang, and C. Dang, "Single-shot multispectral imaging with a monochromatic camera," Optica **4**(10), 1209 (2017).
12. P. Llull, X. Liao, X. Yuan, J. Yang, D. Kittle, L. Carin, G. Sapiro, and D. J. Brady, "Coded aperture compressive temporal imaging," Opt. Express **21**(9), 10526 (2013).
13. K. MacCabe, K. Krishnamurthy, A. Chawla, D. Marks, E. Samei, and D. Brady, "Pencil beam coded aperture x-ray scatter imaging," Opt. Express **20**(15), 16310 (2012).
14. T. Shirai, T. Setälä, and A. T. Friberg, "Temporal ghost imaging with classical non-stationary pulsed light," J. Opt. Soc. Am. B **27**(12), 2549–2555 (2010).
15. Z. Chen, H. Li, Y. Li, J. Shi, and G. Zeng, "Temporal ghost imaging with a chaotic laser," Opt. Eng. **52**(7), 076103 (2013).
16. P. Ryczkowski, M. Barbier, A. T. Friberg, J. M. Dudley, and G. Genty, "Ghost imaging in the time domain," Nat. Photonics **10**(3), 167–170 (2016).
17. F. Devaux, P.-A. Moreau, S. Denis, and E. Lantz, "Computational temporal ghost imaging," Optica **3**(7), 698–701 (2016).
18. A. P. Mosk, A. Lagendijk, G. Lerosey, and M. Fink, "Controlling waves in space and time for imaging and focusing in complex media," Nat. Photonics **6**(5), 283–292 (2012).
19. M. Plöschner, T. Tyc, and T. Čižmár, "Seeing through chaos in multimode fibres," Nat. Photonics **9**(8), 529–535 (2015).
20. Y. Choi, C. Yoon, M. Kim, T. D. Yang, C. Fang-Yen, R. R. Dasari, K. J. Lee, and W. Choi, "Scanner-free and wide-field endoscopic imaging by using a single multimode optical fiber," Phys. Rev. Lett. **109**(20), 203901 (2012).
21. T. Čižmár and K. Dholakia, "Exploiting multimode waveguides for pure fibre-based imaging," Nat. Commun. **3**(1), 1027 (2012).

22. B. Redding, S. Popoff, and H. Cao, "Using a Multimode Fiber as a High Resolution, Low Loss Spectrometer," Opt. Lett. **37**(16), 3384–3386 (2012).
23. S. M. Kolenderska, O. Katz, M. Fink, and S. Gigan, "Scanning-free imaging through a single fiber by random spatio-spectral encoding," Opt. Lett. **40**(4), 534 (2015).
24. B. Redding, M. Alam, M. Seifert, and H. Cao, "High-resolution and broadband all-fiber spectrometers," Optica **1**(3), 175 (2014).
25. W. Xiong, S. Gertler, H. Yilmaz, and H. Cao, "Multimode fiber based single-shot full-field measurement of optical pulses," arXiv 1907.09057, (2019).
26. C. G. Amiot, P. Ryczkowski, A. T. Friberg, J. M. Dudley, and G. Genty, "Ghost optical coherence tomography," Opt. Express **27**(17), 24114–24122 (2019).
27. P. C. Hansen, "The L-Curve and Its Use in the Numerical Treatment of Inverse Problems" *Computational Inverse Problems in Electrocardiology* WIT Press, 119–142(2000).
28. W. Xiong, P. Ambichl, Y. Bromberg, B. Redding, S. Rotter, and H. Cao, "Principal modes in multimode fibers: exploring the crossover from weak to strong mode coupling," Opt. Express **25**(3), 2709–2724 (2017).
29. C. Hauger, M. Wörz, and T. Hellmuth, "Interferometer for optical coherence tomography," Appl. Opt. **42**(19), 3896–3902 (2003).
30. P. Koch, V. Hellemanns, and G. Hüttmann, "Linear optical coherence tomography system with extended measurement range," Opt. Lett. **31**(19), 2882–2884 (2006).
31. Y. Choi, T. D. Yang, K. J. Lee, and W. Choi, "Full-field and single-shot quantitative phase microscopy using dynamic speckle illumination," Opt. Lett. **36**(13), 2465–2467 (2011).